

## Stimulated Raman spectroscopy of $^{13}\text{CF}_4$

R.Z. Martínez<sup>a</sup>, D. Bermejo<sup>a</sup>, V. Boudon<sup>b,\*</sup>

<sup>a</sup> Instituto de Estructura de la Materia, IEM-CSIC, Serrano 123, E-28006 Madrid, Spain

<sup>b</sup> Laboratoire Interdisciplinaire Carnot de Bourgogne, UMR 6303 CNRS – Université Bourgogne Franche-Comté, 9 Av. A. Savary, BP 47870, F-21078 Dijon Cedex, France

### ARTICLE INFO

#### Article history:

Received 30 August 2017

In revised form 18 October 2017

Accepted 19 October 2017

Available online 20 October 2017

#### Keywords:

Carbon tetrafluoride

Stimulated Raman spectroscopy

Cold and hot bands

Rovibrational structure

Isotopologue

### ABSTRACT

$\text{CF}_4$  is a powerful greenhouse gas, mostly released in the atmosphere by industries. A careful modeling of its absorption spectrum is required in order to allow accurate atmospheric concentration measurements. For this aim, high resolution Raman spectroscopy is of great help, since it gives access to rovibrational levels that are not directly reachable through dipolar absorption, although they are involved in hot band generation. Following our previous work on  $^{12}\text{CF}_4$ , we present here a similar investigation of the second isotopologue,  $^{13}\text{CF}_4$ . The spectra of the  $v_1$  ( $909.21\text{ cm}^{-1}$ ),  $2v_1 - v_1$  ( $906.77\text{ cm}^{-1}$ ),  $v_1 + v_2 - v_2$  ( $909.33\text{ cm}^{-1}$ ),  $v_2$  ( $435.47\text{ cm}^{-1}$ ),  $2v_2$  ( $868.10\text{ cm}^{-1}$ ) and  $3v_2 - v_2$  ( $865.73\text{ cm}^{-1}$ ) bands were obtained with a quasi-continuous wave stimulated Raman spectrometer. These six bands were studied at temperatures of 140 and 298 K (for the hot bands). These spectra could be assigned and modeled thanks to the XTDS and SPVIEW software developed in the Dijon group.

© 2017 Elsevier Inc. All rights reserved.

## 1. Introduction

Tetrafluoromethane ( $\text{CF}_4$ ), also known as Halocarbon 14, PFC-14 or R-14, is a colorless, non-toxic, non-flammable, non-corrosive gas belonging to the group of perfluorocarbons (PFCs). Its role in the field of Earth's climate change as a strong greenhouse gas [1–6] has been described in our previous papers [7–11]. These ones were devoted to the main isotopologue, namely  $^{12}\text{CF}_4$ . Our recent global study [10] allows a better simulation of most part of the atmospheric absorption of this species.

For a given molecule, however, gathering high-resolution spectroscopic data about different isotopologues, and not only the main one, is of importance to obtain accurate and reliable data concerning the species's potential energy surface. This is why we also undertook a spectroscopic investigation of  $^{13}\text{CF}_4$  (1.1% in natural abundance). We start here with a high-resolution stimulated Raman investigation, similar to what we performed for the main isotopologue in Ref. [9]. To our knowledge,  $^{13}\text{CF}_4$  has never been investigated in detail up to now, and certainly not using Raman spectroscopy. In the case of molecules with no permanent dipole moment, this technique allows to retrieve important data about rovibrational levels that are not accessible through direct absorption techniques, at least in first approximation.

Section 2 details the experimental setup and data. Section 3 recalls the effective Hamiltonian model we use for spherical-top

molecules with  $T_d$  point group symmetry. Then in Section 4 we present and discuss the assignment and fit results.

## 2. Experimental details

The sample of  $^{13}\text{CF}_4$  was purchased from Aldrich with a 99% purity in  $^{13}\text{C}$ . The spectra were recorded by means of a stimulated Raman spectrometer that has been thoroughly described in multiple publications [9,12–14] and it is schematized on Fig. 1. It follows a quasi-cw scheme in which the sample is simultaneously excited by two laser beams (pump and probe) while the frequency of one of them (pump) is scanned. When the frequency difference of the two beams matches the frequency of a Raman-allowed transition of the molecule under study, an energy transfer takes place from the high-frequency to the low-frequency beam. By monitoring the intensity of one of the beams (probe), a high-resolution Raman spectrum of the sample can be obtained.

The fixed-frequency probe beam is generated by a single-mode, cw  $\text{Ar}^+$  laser whose frequency is actively stabilized and locked to a hyperfine transition of  $^{130}\text{Te}_2$  by means of a double feedback loop. The tunable pulsed pump beam is generated by amplifying the cw output of a single-mode ring dye laser in an optical amplifier, which is in turn pumped by a pulsed, single-mode Nd:YAG laser. The pulses emerging from the amplifier have the temporal characteristics of the Nd:YAG laser ( $\sim 12\text{ ns FWHM}$ ) and a Fourier-limited spectral width of  $\sim 60\text{ MHz}$ . This figure, much larger than the linewidth of the probe laser ( $<1\text{ MHz}$ ), defines the spectral resolution of the spectrometer.

\* Corresponding author.

E-mail address: [vincent.boudon@u-bourgogne.fr](mailto:vincent.boudon@u-bourgogne.fr) (V. Boudon).



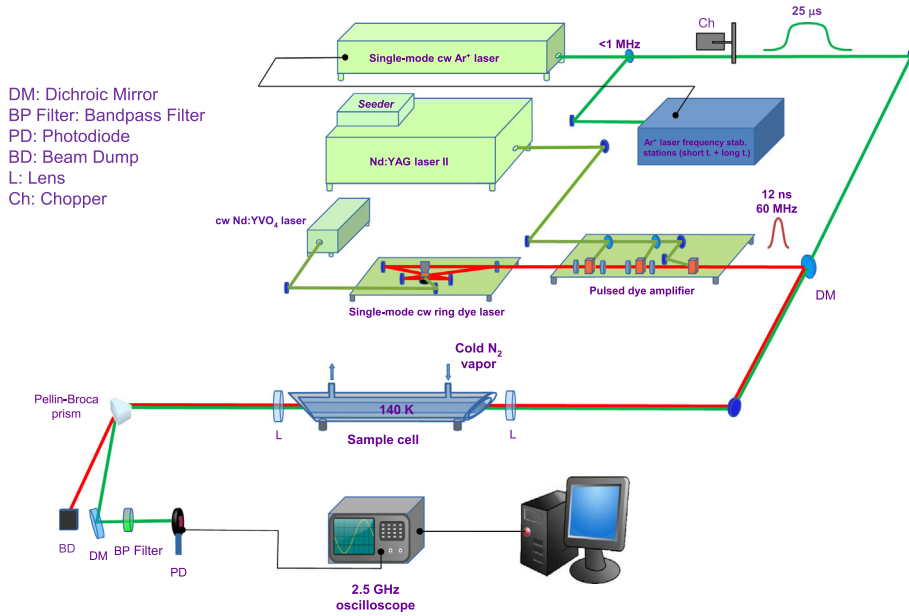


**Fig. 1.** High-resolution stimulated Raman experimental setup.

The recording of the  $\nu_2$  band required replacing the cw Ar<sup>+</sup> laser with a second cw dye laser in order to be able to reach the frequency region where this band lies.

Six bands, identified as  $\nu_1$ ,  $\nu_1 + \nu_2 - \nu_2$ ,  $\nu_2$ ,  $2\nu_2$ ,  $2\nu_1 - \nu_1$  and  $3\nu_2 - \nu_2$  were recorded under the following conditions of pressure and temperature:

- The  $\nu_1$  totally symmetric band Q branch at  $\sim 908\text{ cm}^{-1}$  was recorded at both room temperature (298 K, 4 mbar) and low temperature (140 K, 2.3 mbar). This spectrum also features the  $\nu_1 + \nu_2 - \nu_2$ , at room temperature.
- The  $\nu_2$  band, consisting of an OPOQS branch structure and centered at  $\sim 435\text{ cm}^{-1}$ , was recorded at 140 K and pressures of 8 mbar (for the more intense Q branch) and 20 mbar (for the weaker O, P, R and S branches).
- The  $2\nu_2$  overtone Q branch at  $\sim 868\text{ cm}^{-1}$  was recorded at 298 and 140 K with pressures of 27 and 15 mbar respectively.
- The  $2\nu_1 - \nu_1$  hot band Q branch at  $\sim 907\text{ cm}^{-1}$  was recorded at 298 K and 10 mbar.
- The  $3\nu_2 - \nu_2$  hot band Q branch at  $\sim 868\text{ cm}^{-1}$  was recorded at 298 K and a pressure of 21 mbar.

All the spectra of the different bands were recorded at least twice and averaged in order to improve the signal-to-noise ratio.

### 3. Theoretical model

To model the spectrum, we use the theoretical model based on the tensorial formalism developed by the Dijon group [15–17]. It takes full advantage of the molecule's high symmetry. The basic principles of this approach, applied to CF<sub>4</sub>, have been recalled in our recent paper about the global analysis of this molecule [10]. We outline here the main elements that are necessary for the present study.

CF<sub>4</sub>, just like CH<sub>4</sub> and other tetrahedral spherical top molecules, possesses four normal modes of vibration: one non-degenerate mode with  $A_1$  symmetry ( $\nu_1$ ), one doubly-degenerate mode with  $E$  symmetry ( $\nu_2$ ), and two triply-degenerate modes with  $F_2$  sym-

metry ( $\nu_3$  and  $\nu_4$ ). Only  $F_2$  fundamentals are infrared active, in first approximation, while all modes are Raman active.

The formalism used here allows a systematic expansion of the Hamiltonian and transition moment operators up to a given order and for any or group of vibrational levels or polyad. If we consider an XY<sub>4</sub> molecule for which the vibrational levels are grouped into a series of polyads designed by  $P_k$  ( $k = 0, \dots, n$ ),  $P_0$  being the ground state (GS), the Hamiltonian operator can be put in the following form (after performing some contact transformations):

$$\mathcal{H} = \mathcal{H}_{\{P_0\text{GS}\}} + \mathcal{H}_{\{P_1\}} + \dots + \mathcal{H}_{\{P_k\}} + \dots + \mathcal{H}_{\{P_{n-1}\}} + \mathcal{H}_{\{P_n\}}. \quad (1)$$

Terms like  $\mathcal{H}_{\{P_k\}}$  contain rovibrational operators which have no matrix element within the  $P_{k'<k}$  basis sets. The effective Hamiltonian for polyad  $P_n$  is obtained by projecting  $\mathcal{H}$  in the  $P_n$  Hilbert subspace, i.e.

$$\begin{aligned} H^{(P_n)} &= P^{(P_n)} \mathcal{H} P^{(P_n)} \\ &= H_{\{GS\}}^{(P_n)} + H_{\{P_1\}}^{(P_n)} + \dots + H_{\{P_k\}}^{(P_n)} + \dots + H_{\{P_{n-1}\}}^{(P_n)} + H_{\{P_n\}}^{(P_n)}. \end{aligned} \quad (2)$$

The different terms are written in the form

$$\mathcal{H}_{\{P_k\}} = \sum_{\text{all indexes}} t_{\{s\}\{s'\}}^{\Omega(K,n\Gamma)\Gamma_v\Gamma'_v} \beta \left[ {}^e V_{\{s\}\{s'\}}^{\Omega_v(\Gamma_v\Gamma'_v)\Gamma} \otimes R^{\Omega(K,n\Gamma)} \right]^{(A_1)}. \quad (3)$$

In this equation, the  $t_{\{s\}\{s'\}}^{\Omega(K,n\Gamma)\Gamma_v\Gamma'_v}$  are the parameters to be determined, while  ${}^e V_{\{s\}\{s'\}}^{\Omega_v(\Gamma_v\Gamma'_v)\Gamma}$  and  $R^{\Omega(K,n\Gamma)}$  are vibrational and rotational operators of respective degree  $\Omega_v$  and  $\Omega$ . Their construction is described in Ref. [15]. Again, the vibrational operators only have matrix elements within the  $P_{k'<k}$  basis sets.  $\beta$  is a factor that allows the scalar terms ( $\Gamma = A_1$ ) to match the usual terms like  $B_0 J^2$ , etc. The order of each individual term is defined as  $\Omega + \Omega_v - 2$ . The correspondence between the Hamiltonian parameters in this formalism and “usual” notations of other authors can be found in [15] and are explicated for the bands of the present study in Tables 1 and 3 below (see next Section).

Such a Hamiltonian development scheme enables the treatment of any polyad system. To consider the various Raman bands of the present study, we need the following effective Hamiltonians:

**Table 1**

Effective Hamiltonian parameter values for ground state,  $v_1 = 1$  and  $v_1 = 2$  levels of  $^{13}\text{CF}_4$ . The standard deviation is given in parentheses, in the unit of the last two digits. The ground state parameters are fixed to the values of  $^{12}\text{CF}_4$ .

Level	Order	$\Omega(K, nC)$	$\{s\} C_1$	$\{s'\} C_2$	Value/cm <sup>-1</sup>	"Usual" notation <sup>b</sup>
GS	0	2(0, 0A <sub>1</sub> )	0000A <sub>1</sub>	0000A <sub>1</sub>	1.9119582	$\times 10^{-1}$ <sup>a</sup> $B_0$
GS	2	4(0, 0A <sub>1</sub> )	0000A <sub>1</sub>	0000A <sub>1</sub>	-6.380	$\times 10^{-8}$ <sup>a</sup> $-D_0$
GS	2	4(4, 0A <sub>1</sub> )	0000A <sub>1</sub>	0000A <sub>1</sub>	-3.433	$\times 10^{-9}$ <sup>a</sup> $-(\sqrt{15}/4\sqrt{2})D_{0t}$
GS	4	6(0, 0A <sub>1</sub> )	0000A <sub>1</sub>	0000A <sub>1</sub>	2.30	$\times 10^{-12}$ <sup>a</sup> $H_0$
GS	4	6(4, 0A <sub>1</sub> )	0000A <sub>1</sub>	0000A <sub>1</sub>	-1.902	$\times 10^{-13}$ <sup>a</sup> $(3\sqrt{5}/16\sqrt{2})H_{4t}$
GS	4	6(6, 0A <sub>1</sub> )	0000A <sub>1</sub>	0000A <sub>1</sub>	-1.010	$\times 10^{-13}$ <sup>a</sup> $-(\sqrt{231}/64\sqrt{2})H_{4t}$
GS	6	8(0, 0A <sub>1</sub> )	0000A <sub>1</sub>	0000A <sub>1</sub>	8.544	$\times 10^{-16}$ <sup>a</sup> $-L_0$
GS	6	8(4, 0A <sub>1</sub> )	0000A <sub>1</sub>	0000A <sub>1</sub>	4.654	$\times 10^{-17}$ <sup>a</sup> $-(3\sqrt{15}/64\sqrt{2})L_{4t}$
GS	6	8(6, 0A <sub>1</sub> )	0000A <sub>1</sub>	0000A <sub>1</sub>	-1.054	$\times 10^{-17}$ <sup>a</sup> $(3\sqrt{77}/256\sqrt{2})L_{6t}$
GS	6	8(8, 0A <sub>1</sub> )	0000A <sub>1</sub>	0000A <sub>1</sub>	4.73	$\times 10^{-19}$ <sup>a</sup> $(1/32\sqrt{33})L_{8t}$
$v_1 = 1$	0	0(0, 0A <sub>1</sub> )	1000A <sub>1</sub>	1000A <sub>1</sub>	909.208279(11)	$v_1$
$v_1 = 1$	2	2(0, 0A <sub>1</sub> )	1000A <sub>1</sub>	1000A <sub>1</sub>	-3.47657(19)	$B_1 - B_0$
$v_1 = 1$	4	4(0, 0A <sub>1</sub> )	1000A <sub>1</sub>	1000A <sub>1</sub>	2.571(83)	$-(D_1 - D_0)$
$v_1 = 1$	4	4(4, 0A <sub>1</sub> )	1000A <sub>1</sub>	1000A <sub>1</sub>	-1.53(13)	$-(\sqrt{15}/4\sqrt{2})(D_{1t} - D_{0t})$
$v_1 = 1$	6	6(0, 0A <sub>1</sub> )	1000A <sub>1</sub>	1000A <sub>1</sub>	-1.829(93)	$\times 10^{-14}$ $H_1 - H_0$
$v_1 = 1$	6	6(6, 0A <sub>1</sub> )	1000A <sub>1</sub>	1000A <sub>1</sub>	-4.48(12)	$\times 10^{-15}$
$v_1 = 1$	6	6(6, 0A <sub>1</sub> )	1000A <sub>1</sub>	1000A <sub>1</sub>	-1.95(42)	$\times 10^{-16}$
$v_1 = 2$	2	0(0, 0A <sub>1</sub> )	2000A <sub>1</sub>	2000A <sub>1</sub>	-2.434882(17)	$2X_{11}$
$v_1 = 2$	4	2(0, 0A <sub>1</sub> )	2000A <sub>1</sub>	2000A <sub>1</sub>	-2.8600(23)	$B_{11} - B_1$
$v_1 = 2$	6	4(0, 0A <sub>1</sub> )	2000A <sub>1</sub>	2000A <sub>1</sub>	4.382(64)	$\times 10^{-10}$ $-(D_{11} - D_1)$
$v_1 = 2$	6	4(4, 0A <sub>1</sub> )	2000A <sub>1</sub>	2000A <sub>1</sub>	-6.6(9.2)	$\times 10^{-13}$ $-(\sqrt{15}/4\sqrt{2})(D_{11t} - D_{1t})$

<sup>a</sup> Fixed value.

<sup>b</sup> The "11" index stands for  $v_1 = 2$ , e.g.  $B_{11}$  is the  $v_1 = 2$  rotational constant.

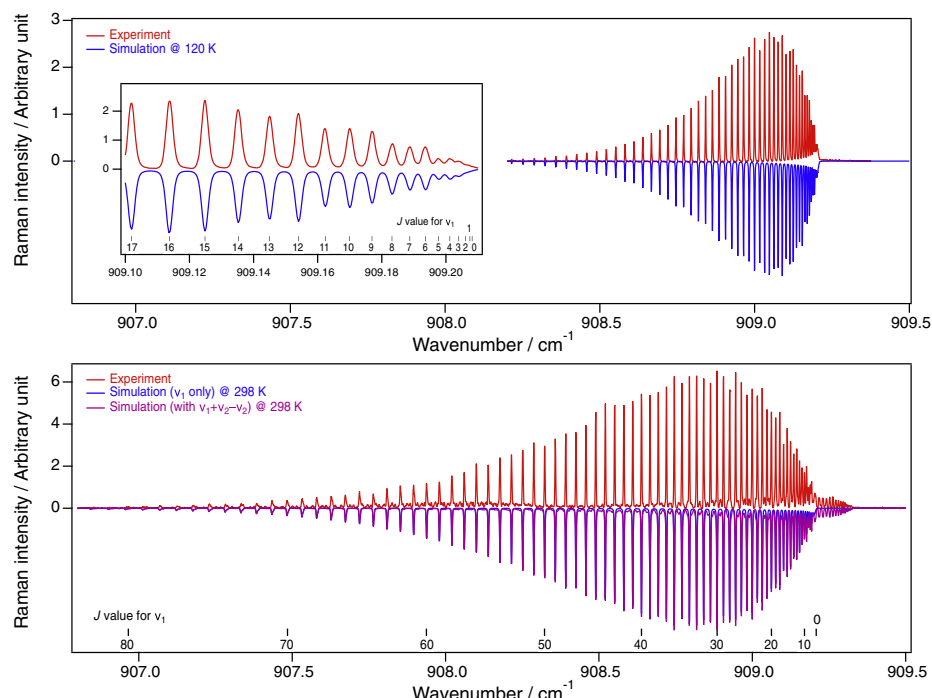


**Fig. 2.** The  $v_1$  experimental spectrum at 140 K (top panel, see text for comments about the lower simulation temperature) and 298 K (bottom panel), compared to the simulation. The insert in the top panel shows a detail in the low- $J$  region. The bottom panel also features the  $v_1 + v_2 - v_2$  hot band (see text).  $J$  values for the  $v_1$  line clusters are indicated.

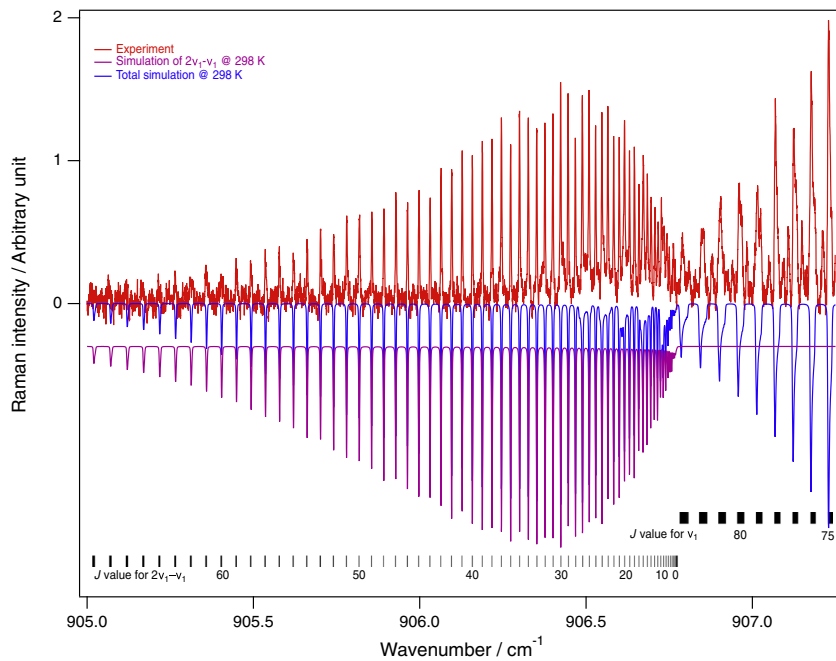


**Fig. 3.** The  $2v_1 - v_1$  region experimental spectrum at 298 K, compared to the simulation with the hot band only and with both the hot and cold bands.  $J$  values and line positions are indicated.

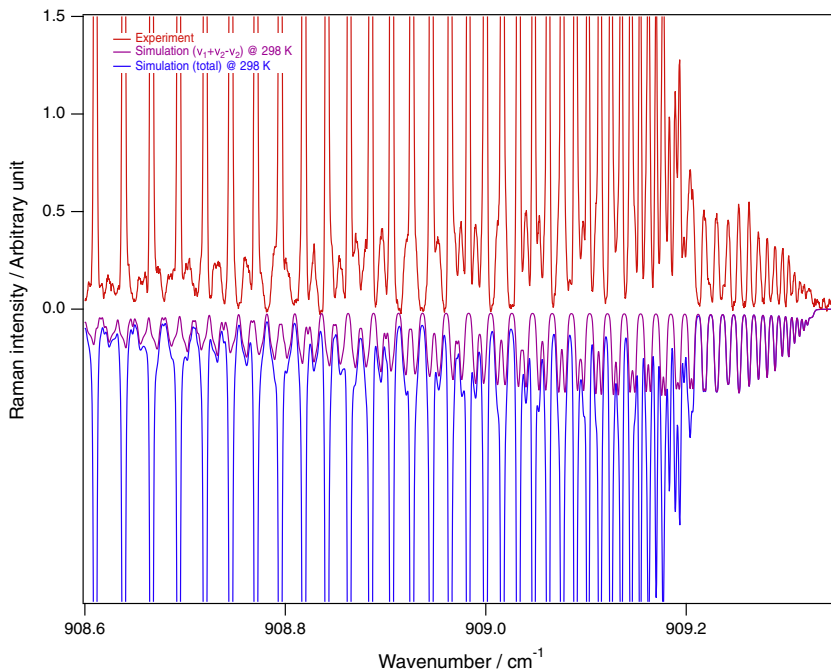


**Fig. 4.** The  $v_1 + v_2 - v_2$  region in the  $v_1$  experimental spectrum at 298 K, compared to the simulation with the hot band only and with both the hot and cold bands.

**Table 2**  
Effective Hamiltonian parameter values for  $v_1 = v_2 = 1$ . The standard deviation is given in parentheses, in the unit of the last two digits. The ground state parameters are fixed to the values of  $^{12}\text{CF}_4$  and are not reported here.

Level	Order	$\Omega(K, nC)$	$\{s\} C_1$	$\{s'\} C_2$	Value / $\text{cm}^{-1}$	"Usual" notation
$v_1 = v_2 = 1$	2	$0(0, 0A_1)$	$1100E$	$1100E$	$1.20013(20)$	$\times 10^{-1}$
$v_1 = v_2 = 1$	4	$2(0, 0A_1)$	$1100E$	$1100E$	$-1.2184(28)$	$\times 10^{-5}$
$v_1 = v_2 = 1$	4	$2(2, 0E)$	$1100E$	$1100E$	$6.619(33)$	$\times 10^{-6}$

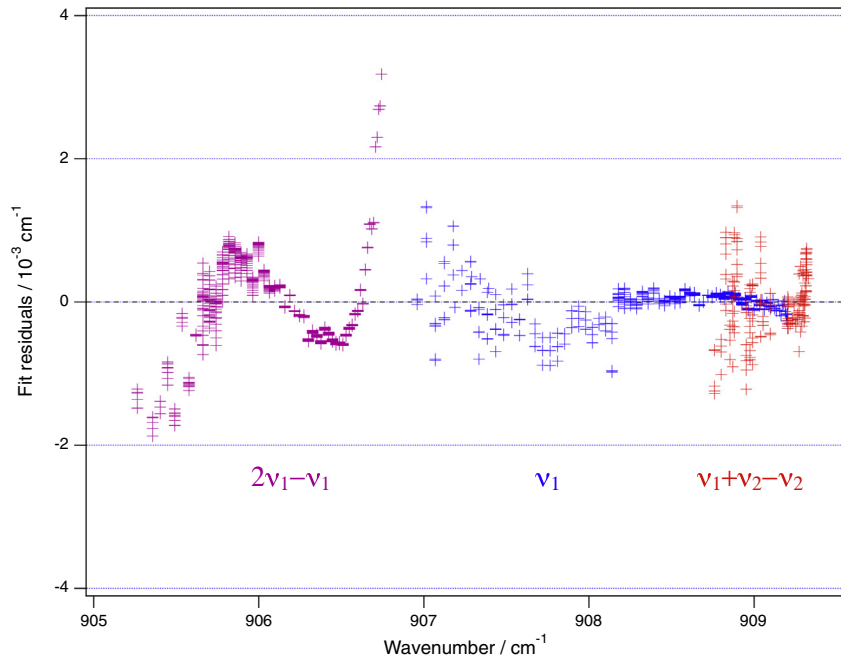


**Fig. 5.** Fit residuals for line positions for the global fit of  $\nu_1$  and  $2\nu_1 - \nu_1$  and for  $\nu_1 + \nu_2 - \nu_2$  (fitted separately).

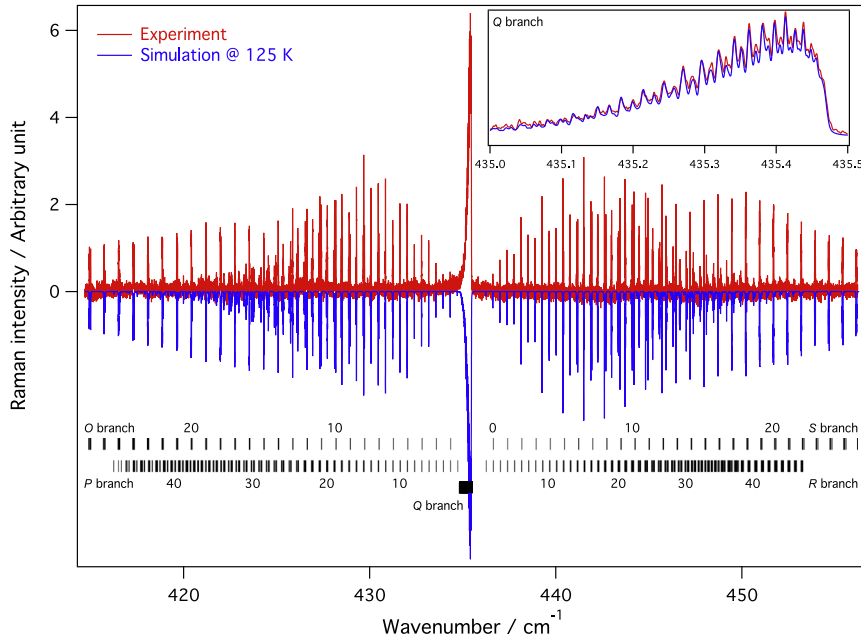


**Fig. 6.** The  $\nu_2$  fundamental band experimental spectrum, compared to the simulation (at 125 K, see text). The insert details the Q branch. Lower state  $J$  values and line positions for the different branches are indicated.

- The ground state effective Hamiltonian,

$$H^{(\text{GS})} = H_{\{\text{GS}\}}^{(\text{GS})}. \quad (4)$$

- The  $\nu_1$  effective Hamiltonian,

$$H^{(\nu_1)} = H_{\{\text{GS}\}}^{(\nu_1)} + H_{\{\nu_1\}}^{(\nu_1)}. \quad (5)$$

- The  $2\nu_1$  effective Hamiltonian,

$$H^{(2\nu_1)} = H_{\{\text{GS}\}}^{(2\nu_1)} + H_{\{\nu_1\}}^{(2\nu_1)} + H_{\{2\nu_1\}}^{(2\nu_1)}. \quad (6)$$

- The  $\nu_1 + \nu_2$  effective Hamiltonian,

$$H^{(\nu_1+\nu_2)} = H_{\{\text{GS}\}}^{(\nu_1+\nu_2)} + H_{\{\nu_2\}}^{(\nu_1+\nu_2)} + H_{\{\nu_1/2\nu_2\}}^{(\nu_1+\nu_2)} + H_{\{\nu_1+\nu_2\}}^{(\nu_1+\nu_2)}. \quad (7)$$

- The  $\nu_2$  effective Hamiltonian,

$$H^{(\nu_2)} = H_{\{\text{GS}\}}^{(\nu_2)} + H_{\{\nu_2\}}^{(\nu_2)}. \quad (8)$$

- The  $2\nu_2$  effective Hamiltonian,

$$H^{(2\nu_2)} = H_{\{\text{GS}\}}^{(2\nu_2)} + H_{\{\nu_2\}}^{(2\nu_2)} + H_{\{2\nu_2\}}^{(2\nu_2)}. \quad (9)$$

- The  $3\nu_2$  effective Hamiltonian,

$$H^{(3\nu_2)} = H_{\{GS\}}^{(3\nu_2)} + H_{\{\nu_2\}}^{(3\nu_2)} + H_{\{2\nu_2\}}^{(3\nu_2)} + H_{\{3\nu_2\}}^{(3\nu_2)}. \quad (10)$$

In order to compute line intensities and to obtain simulated spectra, a polarizability operator is expanded in the same way (see for instance [15] for details about its construction). Since at present we do not consider absolute Raman intensities, the polarizability operator is developed up to the zero order only. In each case under consideration, this amounts to a single isotropic parameter that was simply fixed to 1.

We use here vibrational basis sets restricted to the  $\nu_1$  and  $\nu_2$  modes:

$$|\Psi_{\nu_1}^{(A_1)}\rangle \text{ and } |\Psi_{\nu_2}^{(l_2, C_2)}\rangle, \quad (11)$$

i.e. we use a one-dimensional harmonic oscillator wavefunction for the non-degenerate mode  $\nu_1$  and a two-dimensional one for the doubly degenerate mode  $\nu_2$  with vibrational angular momentum

$l_2$  and  $T_d$  symmetry  $C_2$ . The Hamiltonian and dipole moment matrix elements are calculated in the coupled rovibrational basis sets:

$$\left| \left[ \Psi_{\nu_1}^{(A_1)} \otimes \Psi_r^{(J, nC_r)} \right]_{(C=C_r)} \right\rangle \text{ and } \left| \left[ \Psi_{\nu_2}^{(l_2, C_2)} \otimes \Psi_r^{(J, nC_r)} \right]_{(C=C_2 \otimes C_r)} \right\rangle, \quad (12)$$

$\Psi_r^{(J, nC_r)}$  being a rotational wavefunction with angular momentum  $J$ , rotational symmetry species  $C_r$  and multiplicity index  $n$  (see [15]), while  $C$  is the overall symmetry species.

#### 4. Assignment and fitting of spectra

In order to assign and fit the present  $^{13}\text{CF}_4$  spectra, we expanded all the effective Hamiltonian parts given in Section 3 up to order 6, although, in the end, not all the resulting rovibrational parameters were fitted, as described in the following paragraphs.

In all cases, we started from the  $^{12}\text{CF}_4$  effective Hamiltonian parameters obtained in our most recent study [10] and applied a shift on the band center in order to match the Q branch position. The other effective Hamiltonian parameters showing only small variations when switching from  $^{12}\text{CF}_4$  to  $^{13}\text{CF}_4$ , the initial spectrum

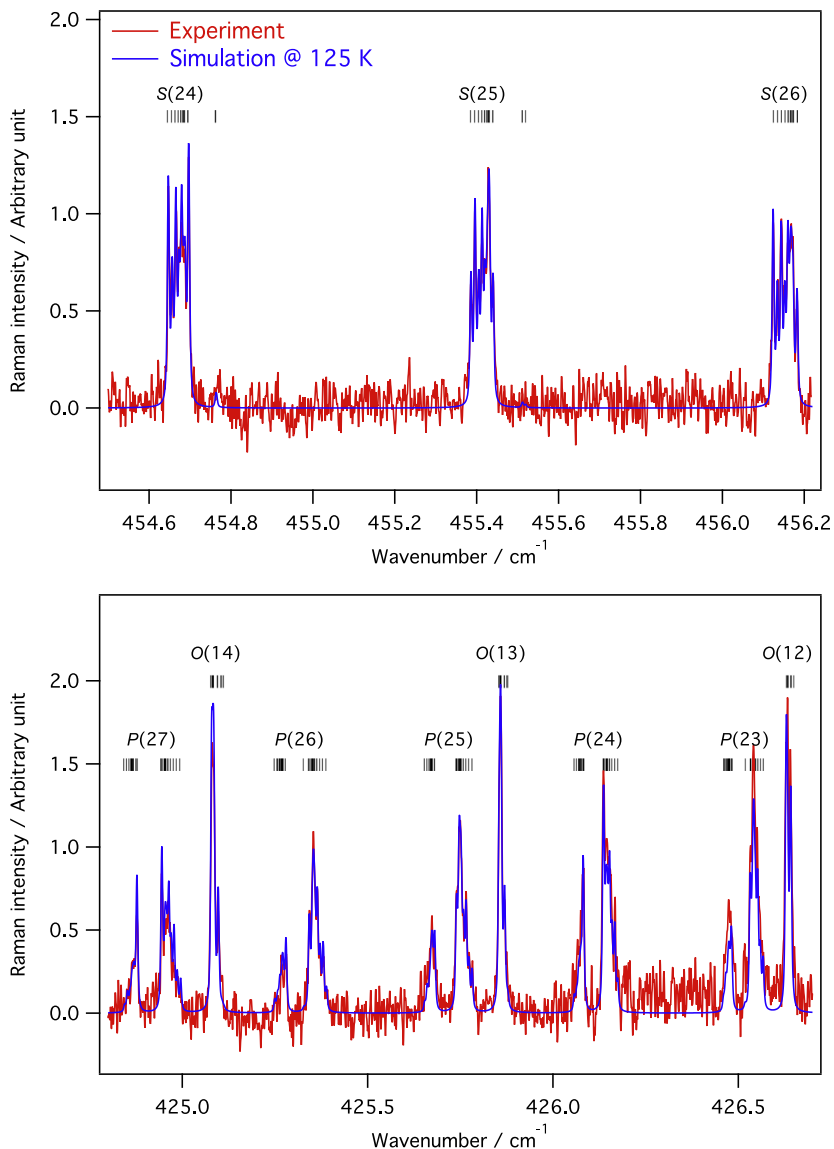


**Fig. 7.** Details in the  $\nu_2$  fundamental band experimental spectrum, compared to the simulation (at 125 K, see text): S branch (top panel) and O and P branches (bottom panel). Lower state  $J$  values and line positions for some clusters are indicated.

simulations performed in this way were already close to the experimental spectra and the assignment was straightforward. The ground state (GS) parameters were always kept fixed to the  $^{12}\text{CF}_4$  values, since we do not have, at present, specific data for this state of  $^{13}\text{CF}_4$ , contrary to the main isotopologue case [11]. But GS values are generally almost independent of the isotopologue.

Just as explained in Ref. [10], we did not set up a global polyad scheme since this is not an easy task in the case of  $\text{CF}_4$  for which the fundamental wavenumbers do not follow simple ratios between all them. Moreover, the present study is only partial, considering only the Raman bands. Such a global description would be a further step after also studying  $^{13}\text{CF}_4$ 's infrared spectrum. Thus, here we only fit together  $\nu_1$  and  $2\nu_1 - \nu_1$  on the one hand, and  $\nu_2$  and  $2\nu_2$  on the other hand, while  $\nu_1 + \nu_2 - \nu_2$  is fitted separately and  $3\nu_2 - \nu_2$  is only extrapolated.

Line assignments, fits and spectrum simulations were performed using the SPVIEW and XTDIS softwares developed in the Dijon group [18]. More specifically, calculations use the STDS package of XTDIS, which is dedicated to tetrahedral  $\text{XY}_4$  molecules [19].

#### 4.1. The $\nu_1$ fundamental band

As usual, the isotropic Raman spectrum of the  $\nu_1$  totally symmetric stretching mode consists of a single Q branch. It is a comb of line clusters, expanding towards lower wavenumbers: each rotational quantum number  $J$  value corresponds to several individual lines that cannot be resolved under the present conditions, except for high  $J$  values for which the tetrahedral splitting (due to the molecule's symmetry) starts to appear.

**Fig. 2** compares the experiment and the simulation for both temperatures at which the spectra were recorded (see Section 2). The room temperature simulation also includes the  $\nu_1 + \nu_2 - \nu_2$  hot band which is described in the next paragraph below. As it can be seen, we could obtain very good spectrum simulations. As for the cold spectrum, the simulation temperature was adjusted to 120 K to better match the intensity profile (see also the discussion about Raman experimental and simulation temperatures in Section 4.4 below). **Table 1** gives the resulting effective Hamiltonian parameters for the  $\nu_1 = 1$  state as obtained from the global fit that we describe hereafter.

#### 4.2. The $2\nu_1 - \nu_1$ hot band and the $\nu_1$ global fit

**Fig. 3** shows the simulation we could obtain for the  $2\nu_1 - \nu_1$  hot band, which also consists of a single Q branch, shifted from the hot band by ca.  $-2.43\text{ cm}^{-1}$  towards lower wavenumbers. It overlaps with high  $J$  line clusters from the  $\nu_1$  cold band.

We performed a global fit of the  $\nu_1 = 1$  and  $\nu_1 = 2$  levels. The resulting effective Hamiltonian parameters were used for the simulations of **Figs. 2 and 3** and are given in **Table 1**. We can see that the sextic parameters for  $\nu_1 = 1$  largely differ from those of  $^{12}\text{CF}_4$  from Ref. [10]. The reason is that in this reference, the  $\nu_1$  band was included in a more global fit, implying more bands, so it is difficult to compare fitted high-order terms from both studies; however, we choose to give here the parameter set giving the best  $^{13}\text{CF}_4$  fit, rather than fixing some parameters to  $^{12}\text{CF}_4$  values.

#### 4.3. The $\nu_1 + \nu_2 - \nu_2$ hot band

**Fig. 4** displays a detail on the  $\nu_1 + \nu_2 - \nu_2$  hot band, which was already visible in the bottom panel of **Fig. 2**. Although this hot band, which is slightly shifted towards higher wavenumbers (ca.  $+0.12\text{ cm}^{-1}$ ), compared to the cold band, strongly overlaps with this one, its Q branch was quite easy to assign. Again, the resulting simulation is quite convincing.

As explained before, this hot band was fitted separately, with the  $\nu_1 = 1$  and  $\nu_2 = 1$  effective Hamiltonian parameters fixed to the values obtained from the  $\nu_1/2\nu_1 - \nu_1$  global fit (see above) and from the  $\nu_2/2\nu_2$  global fit (see below), respectively. The  $\nu_1 = \nu_2 = 1$  resulting parameters are given in **Table 2**. It should be mentioned that in the polyad scheme used here and described in Section 3 (see Eq. (7)), the  $\nu_2 = 2$  and  $\nu_1 = 1$  form an interacting Dyad. However, no interaction parameter between these two levels could be determined here and they were kept fixed to zero.

**Fig. 5** displays the fit residuals for line positions for  $\nu_1$ ,  $2\nu_1 - \nu_1$  and  $\nu_1 + \nu_2 - \nu_2$ . It can be seen that the  $2\nu_1 - \nu_1$  residuals exhibit a systematic polynomial deviation, although they stay quite small. This behavior could be corrected with a higher order term, but this may not be physically meaningful. Rather, this more likely requires, as we did recently in the  $^{12}\text{CF}_4$  case for the same reason, a slight refinement of GS parameter values. We will attempt this when adding infrared absorption data in a future study.

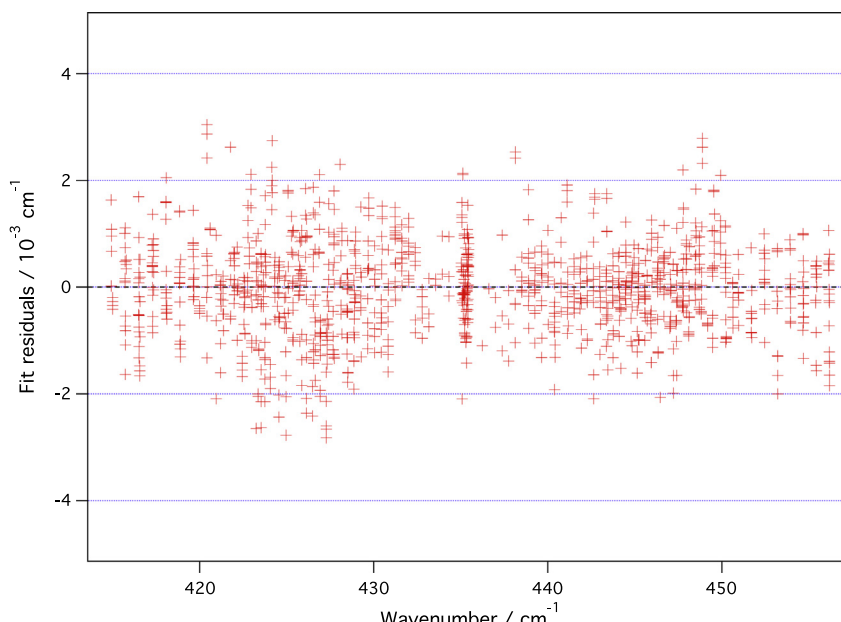


**Fig. 8.** Fit residuals for line positions for the  $\nu_2$  fundamental band.

#### 4.4. The $v_2$ fundamental band

The anisotropic Raman spectrum of the doubly degenerate  $v_2$  bending fundamental band possesses a nice structure with  $O(\Delta J = -2)$ ,  $P(\Delta J = -1)$ ,  $Q(\Delta J = 0)$ ,  $R(\Delta J = +1)$  and  $S(\Delta J = +2)$  branches, just as for  $^{12}\text{CF}_4$  [9] or  $\text{SF}_6$  [20,21]. In this case, the tetrahedral splitting is sufficient for the  $J$  clusters to be at least partially resolved. Starting from the  $^{12}\text{CF}_4$  effective Hamiltonian parameter values allowed an easy assignment for  $^{13}\text{CF}_4$ .

**Fig. 6** displays an overview of the band, compared to the simulation. Some details in different branches are shown in **Fig. 7**. The simulations in these two figures result from the global fit described in the next paragraph. It should be noticed that, although the spectrum was recorded at 140 K, the simulation temperature in this case was readjusted to 125 K in order to better match the intensity profile of the different branches of the band, especially for the glo-

bal view of **Fig. 6**. However, this temperature should be considered with caution, as the Raman intensities in such a large spectrum, resulting from the collage of several small wavenumber ranges may not be reliable in stimulated Raman spectroscopy.

**Fig. 8** shows the fit residuals for line positions for this  $v_2$  fundamental band. The effective Hamiltonian parameters are given in **Table 3**.

#### 4.5. The $2v_2$ overtone band and the $v_2$ global fit

Since overtone bands have a much weaker intensity, only the  $Q$  branch of the totally symmetric sublevels can be observed in stimulated Raman spectroscopy. The  $2v_2$  band possesses two sublevels, with respective symmetry  $A_1$  and  $E$  in the  $T_d$  point group. We could observe the  $Q$  branch of the  $A_1$  sublevel, just as in the case of  $^{12}\text{CF}_4$  [9].

**Table 3**  
Effective Hamiltonian parameter values for  $v_2 = 1$ ,  $v_2 = 2$  and  $v_2 = 3$  levels of  $^{13}\text{CF}_4$ . The standard deviation is given in parentheses, in the unit of the last two digits. The ground state parameters are fixed to the values of  $^{12}\text{CF}_4$  and are not reported here.

Level	Order	$\Omega(K, nC)$	$\{s\} C_1$	$\{s'\} C_2$	Value/ cm <sup>-1</sup>	"Usual" notation <sup>c</sup>
$v_2 = 1$	0	$0(0, 0A_1)$	$0100E$	$0100E$	435.473294(53)	$v_2$
$v_2 = 1$	2	$2(0, 0A_1)$	$0100E$	$0100E$	$-3.38427(87)$	$B_2 - B_0$
$v_2 = 1$	2	$2(2, 0E)$	$0100E$	$0100E$	$-1.08013(75)$	$\sqrt{3}b_2 + (24\sqrt{3}/7)C_6$
$v_2 = 1$	3	$3(3, 0A_2)$	$0100E$	$0100E$	$3.072(13)$	$-1/2d_2$
$v_2 = 2$	2	$0(0, 0A_1)$	$0200A_1$	$0200A_1$	$-2.84275(11)$	$A_1$ sublevel
$v_2 = 2$	4	$2(0, 0A_1)$	$0200A_1$	$0200A_1$	$2.383(18)$	$B_{22}^{A_1} - B_2$
$v_2 = 2$	6	$4(0, 0A_1)$	$0200A_1$	$0200A_1$	0.0	$-(D_{22}^{A_1} - D_2)$
$v_2 = 2$	4	$2(2, 0E)$	$0200A_1$	$0200E$	$-2.19$	$\times 10^{-6}$ <sup>b</sup>
$v_2 = 2$	6	$4(2, 0E)$	$0200A_1$	$0200E$	$-2.32$	$\times 10^{-10}$ <sup>c</sup>
$v_2 = 2$	2	$0(0, 0A_1)$	$0200E$	$0200E$	1.414(25)	$E$ sublevel
$v_2 = 2$	4	$2(0, 0A_1)$	$0200E$	$0200E$	$-2.27(14)$	$B_{22}^E - B_2$
$v_2 = 2$	4	$2(0, 0E)$	$0200E$	$0200E$	0.0	<sup>a</sup>
$v_2 = 3$	4	$0(0, 0A_1)$	$0300E$	$0300E$	8.6	$\times 10^{-2}$ <sup>a</sup>
$v_2 = 3$	6	$2(0, 0A_1)$	$0300E$	$0300E$	3.0	$\times 10^{-6}$ <sup>a</sup>

<sup>a</sup> Fixed value.

<sup>b</sup> Fixed to  $^{12}\text{CF}_4$  value.

<sup>c</sup> The "22" index stands for  $v_2 = 2$ , e.g.  $B_{22}^{A_1}$  is the rotational constant for the  $A_1$  sub level of  $v_2 = 2$ .

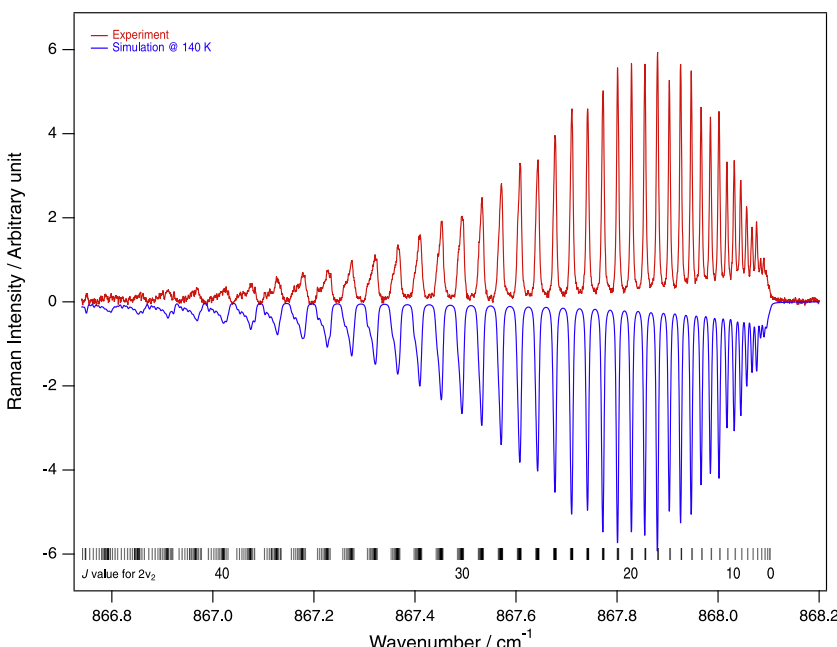


**Fig. 9.** The  $2v_2$  overtone band experimental spectrum ( $A_1$  sublevel), compared to the simulation at 140 K.  $J$  values and line positions are indicated.

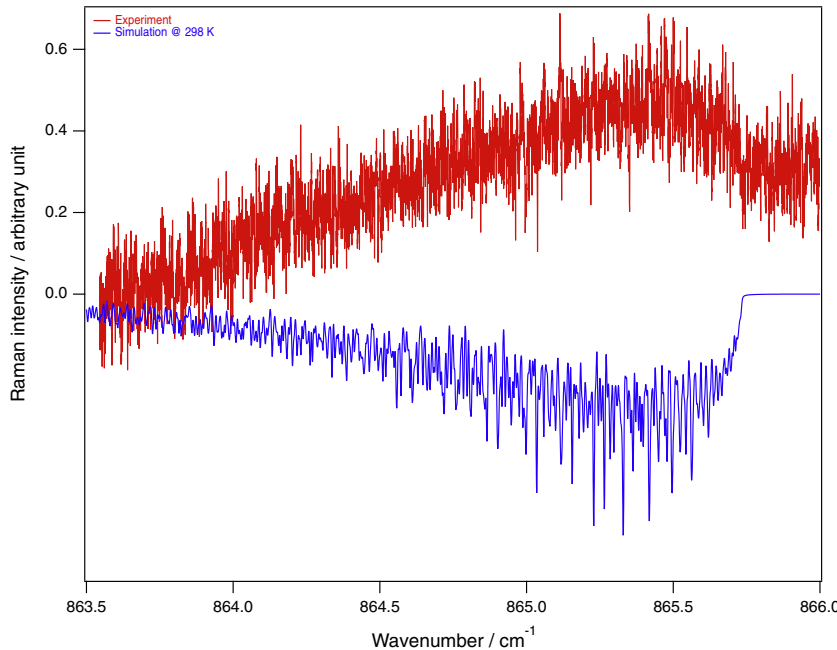


**Fig. 10.** The  $3v_2 - v_2$  hot band experimental spectrum, compared to the extrapolated simulation at 298 K.

**Fig. 9** shows this spectrum, compared with the simulation. Again, we obtain a very good match. The beginning of the tetrahedral splitting is observable in high  $J$  clusters on the left (above  $J = 30$ ).

We performed a global fit of the  $v_2 = 1$  and  $v_2 = 2$  levels, with the resulting effective Hamiltonian parameters given in [Table 3](#). Since, at present, we have less data than for the main isotopologue, some parameters for  $^{13}\text{CF}_4$  could not yet be determined properly and were kept fixed to their  $^{12}\text{CF}_4$  values from Ref. [\[10\]](#). Since there is a coupling between the two sublevels, the position of the  $E$  sublevel can be fitted and it is necessary to obtain a good fit. Nevertheless, the obtained value should be taken with caution, until we can perform a better global fit including infrared absorption data as in Ref. [\[10\]](#).

#### 4.6. Extrapolation to the $3v_2 - v_2$ hot band

The  $3v_2 - v_2$  hot band  $Q$  branch could also be observed, although it is very weak. Contrary to the  $^{12}\text{CF}_4$  [\[9\]](#), it was not possible to resolve its rotational structure. As shown in [Fig. 10](#), we just performed here an extrapolated simulation, using the present effective Hamiltonian parameters for  $v_2 = 1$  and  $v_2 = 2$  and the  $^{12}\text{CF}_4$  values [\[10\]](#) for  $v_2 = 3$ . The result is anyway quite convincing.

#### 4.7. Discussion

[Table 4](#) gives some statistics for the present fits of stimulated Raman data for  $^{13}\text{CF}_4$ . We obtained small root mean square deviations ( $d_{\text{RMS}} < 10^{-3} \text{ cm}^{-1}$ ) for a quite large  $J$  value range.

**Table 4**  
Fit statistics.

Band	Number of data	$J_{\text{max}}$	$d_{\text{RMS}}/10^{-3} \text{ cm}^{-1}$
$v_1$	987	80	0.196
$2v_1 - v_1$	1301	63	0.726
$v_2$	1261	41	0.871
$2v_2$	228	45	0.537
$v_1 + v_2$	174	39	0.501

From the present results and previous references [\[9,10\]](#), we can deduce the isotopic shifts for the  $v_1$  and  $v_2$  fundamental bands:

$$\Delta \tilde{v}_{13-12}(v_1) \simeq +0.1361 \text{ cm}^{-1}/\text{amu}, \quad (13)$$

$$\Delta \tilde{v}_{13-12}(v_2) \simeq +0.0931 \text{ cm}^{-1}/\text{amu}, \quad (14)$$

(amu standing for “atomic mass unit”).

#### 5. Conclusion

We have presented here the first high-resolution spectroscopic study of  $^{13}\text{CF}_4$ , using stimulated Raman spectroscopy. We could obtain reliable spectrum simulations of six rovibrational bands and isotopic shifts for the  $v_1$  and  $v_2$  fundamental bands. These results could be of help to refine the potential energy surface of the  $\text{CF}_4$  molecule. As in our previous works, this shows the usefulness of stimulated Raman spectroscopy that provides important data that can hardly be obtained with other techniques, especially in the case of non-polar molecules.

A next step will be to combine the present Raman data with infrared absorption data in order to obtain a global analysis of  $^{13}\text{CF}_4$  spectra.

#### References

- [1] C.P. Rinsland, E. Mathieu, R. Zander, R. Nassar, P. Bernath, C. Boone, L.S. Chiou, Long-term stratospheric carbon tetrafluoride ( $\text{CF}_4$ ) increase inferred from 1985–2004 infrared space-based solar occultation measurements, *Geophys. Res. Lett.* 33 (2006) L02808.
- [2] R. Zander, M.R. Gunson, C.B. Fanner, C.P. Rinsland, F.W. Irion, E. Mahieu, The 1985 chlorine and fluorine inventories in the stratosphere based on ATMOS observations at 30° north latitude, *J. Atmos. Chem.* 15 (1992) 171–186.
- [3] R. Zander, S. Solomon, E. Mahieu, A. Goldman, C. Rinsland, M.R. Gunson, M.C. Abrams, A.Y. Chang, R.J. Salawitch, H.A. Michelsen, M.J.N. MJ, G.P. Stiller, Increase of stratospheric carbon tetrafluoride ( $\text{CF}_4$ ) based on atmos observations from space, *Geophys. Res. Lett.* 23 (1996) 2353–2356.
- [4] B. Sen, G.C. Toon, J.-F. Blavier, E.L. Fleming, C.H. Jackman, Balloon-borne observations of mid-latitude fluorine abundance, *J. Geophys. Res.* 101 (1996) 9045–9054.
- [5] D.R. Worton, W.T. Sturges, L.K. Gohar, K.P. Shine, P. Martinierie, D.E. Oram, S.P. Humphrey, P. Begley, L. Gunn, J.-M. Barnola, J. Schwander, R. Mulvaney, Atmospheric trends and radiative forcings of  $\text{CF}_4$  and  $\text{C}_2\text{F}_6$  inferred from firn air, *Environ. Sci. Technol.* 41 (2007) 2184–2189.

- [6] J. Mühle, A.L. Ganesan, B.R. Miller, P.K. Salameh, C.M. Harth, B.R. Greally, M. Rigby, L. Porter, L.P. Steele, C.M. Trudinger, P.B. Krummel, S. O'Doherty, P.J. Fraser, P.G. Simmonds, R.G. Prinn, R.F. Weiss, Perfluorocarbons in the global atmosphere: tetrafluoromethane, hexafluoroethane, and octafluoropropane, *Atmos. Chem. Phys.* 10 (2010) 5145–5164.
- [7] V. Boudon, J.-P. Champion, T. Gabard, G. Pierre, M. Loëte, C. Wenger, Spectroscopic tools for remote sensing of greenhouse gases CH<sub>4</sub>, CF<sub>4</sub> and SF<sub>6</sub>, *Environ. Chem. Lett.* 1 (2003) 86–91.
- [8] V. Boudon, J. Mitchell, A. Domanskaya, C. Maul, R. Georges, A. Benidar, W.G. Harter, High-resolution spectroscopy and analysis of the  $\nu_3/2\nu_4$  dyad of CF<sub>4</sub>, *Mol. Phys.* 109 (2011) 2273–2290.
- [9] V. Boudon, D. Bermejo, R.Z. Martínez, High-resolution stimulated Raman spectroscopy and analysis of the  $\nu_1, 2\nu_1 - \nu_1$ ,  $\nu_2, 2\nu_2$ , and  $3\nu_2 - \nu_2$  bands of CF<sub>4</sub>, *J. Raman. Spectrosc.* 44 (2013) 731–738.
- [10] M. Carlos, O. Gruson, C. Richard, V. Boudon, M. Rotger, X. Thomas, C. Maul, C. Sydow, A. Domanskaya, R. Georges, P. Soulard, O. Pirali, M. Goubet, P. Asselin, T.R. Huet, High-resolution spectroscopy and global analysis of CF<sub>4</sub> rovibrational bands to model its atmospheric absorption, *J. Quant. Spectrosc. Radiat. Transfer* 201 (2017) 75–93.
- [11] V. Boudon, M. Carlos, C. Richard, O. Pirali, Pure rotation spectrum of CF<sub>4</sub> in the  $\nu_3 = 1$  state using THz synchrotron radiation, *J. Mol. Spectrosc.* 348 (2018) 43–46, <https://doi.org/10.1016/j.jms.2017.07.010>.
- [12] G.D. Lonardo, L. Fusina, A. Baldan, R.Z. Martínez, D. Bermejo, High resolution infrared and Raman spectroscopy of  $\nu_2$  and associated combination and hot bands of <sup>13</sup>C<sup>12</sup>CD<sub>2</sub>, *Mol. Phys.* 109 (2011) 2533–2542.
- [13] F. Thibault, B. Corretja, A. Viel, D. Bermejo, R. Martínez, B. Bussery-Honvault, Linewidths of C<sub>2</sub>H<sub>2</sub> perturbed by H<sub>2</sub>: experiments and calculations from an *ab initio* potential, *Phys. Chem. Chem. Phys.* 10 (2008) 5419–5428.
- [14] N. Moazzen-Ahmadi, R.Z. Martínez, D. Bermejo, The  $\nu_5$  band of (<sup>12</sup>CH<sub>3</sub>)<sup>13</sup>CH<sub>3</sub>): high resolution stimulated Raman spectrum and global three band analysis, *J. Mol. Spectrosc.* 269 (2011) 151–155.
- [15] J.-P. Champion, M. Loëte, G. Pierre, Spherical top spectra, in: K.N. Rao, A. Weber (Eds.), *Spectroscopy of the Earth's Atmosphere and Interstellar Medium*, Academic Press, San Diego, 1992, pp. 339–422.
- [16] V. Boudon, J.-P. Champion, T. Gabard, M. Loëte, F. Michelot, G. Pierre, M. Rotger, C. Wenger, M. Rey, Symmetry-adapted tensorial formalism to model rovibrational and rovibronic spectra of molecules pertaining to various point groups, *J. Mol. Spectrosc.* 228 (2004) 620–634.
- [17] V. Boudon, J.-P. Champion, T. Gabard, M. Loëte, M.R.C. Wenger, Spherical top theory and molecular spectra, in: M. Quack, F. Merkt (Eds.), *Handbook of High-Resolution Spectroscopy*, Vol. 3, Wiley, Chichester, West Sussex, United Kingdom, 2011, pp. 1437–1460.
- [18] C. Wenger, V. Boudon, M. Rotger, J.P. Sanzharov, J.P. Champion, XTDS and SPVIEW: graphical tools for the analysis and simulation of high-resolution molecular spectra, *J. Mol. Spectrosc.* 251 (2008) 102–113.
- [19] C. Wenger, J.-P. Champion, Spherical top data system (STDS) software for the simulation of spherical top spectra, *J. Quant. Spectrosc. Radiat. Transfer* 59 (1998) 471–480.
- [20] D. Bermejo, R.Z. Martínez, E. Loubignac, V. Boudon, G. Pierre, Simultaneous analysis of the  $\nu_2$  Raman and  $\nu_2 + \nu_6$  infrared spectra of the SF<sub>6</sub> molecule, *J. Mol. Spectrosc.* 201 (2000) 164–171.
- [21] V. Boudon, J.L. Doménech, A. Ramos, D. Bermejo, H. Willner, High-resolution stimulated Raman spectroscopy and analysis of the  $\nu_2$ ,  $\nu_5$  and  $2\nu_6$  bands of <sup>34</sup>SF<sub>6</sub>, *Mol. Phys.* 104 (16–17) (2006) 2653–2661.